Defect-engineered metal-organic frameworks (MOF-808) towards the improved adsorptive removal of organic dyes and chromium (vi) species

NJC

ROYAL SOCIETY OF CHEMISTRY

PAPER

View Article Online
View Journal | View Issue

Cite this: *New J. Chem.*, 2023, **47**, 6433

Defect-engineered metal–organic frameworks (MOF-808) towards the improved adsorptive removal of organic dyes and chromium (VI) species from water†

Khoa D. Nguyen,[ab] Nhi T. Vo,[ab] Khanh T. M. Le,[ab] Khanh V. Ho,[ab] Nam T. S. Phan,[ab] Phuoc H. Ho *[c] and Ha V. Le*[ab]

Received 20th November 2022,
Accepted 28th February 2023

DOI: 10.1039/d2nj05693c

rsc.li/njc

In this work, two defective zirconium-based metal–organic frameworks (Zr-MOFs), MOF-808-OH and MOF-808-NH_2, were synthesized by partially replacing the 1,3,5-benzenetricarboxylate building block with 5-hydroxyisophthalate and 5-aminoisophthalate, respectively. The structural features of the defective materials were analyzed by powder X-ray diffraction (PXRD), scanning electron microscopy (SEM), nitrogen physisorption at 77 K, and thermogravimetric analysis (TGA). Importantly, the number of defect sites determined *via* proton nuclear magnetic resonance (^{1}H-NMR) analysis of the digested materials was approximately 7 mol% for MOF-808-OH and 3 mol% for MOF-808-NH_2. The presence of the defect sites increased the number of acidic centers on Zr-clusters originating from missing-linker nodes which accounted for a remarkable adsorption capacity towards various anionic organic dyes and chromium (VI) species. Compared to standard MOF-808, the defect-engineered ones showed significant increments by 30–60% in trapping capacity for anionic contaminants including sunset yellow, quinoline yellow, methyl orange, and potassium dichromate, while they exhibited modest improvements by 5–15% in the removal of cationic dyes, namely malachite green and methylene blue.

Introduction

Metal–organic frameworks (MOFs) are crystalline materials, constructed by linking metal-containing clusters and organic ligands, yielding open and robust frameworks. Owing to the diversity in pore size and function, exceeding porosity along with high thermal and chemical stability, MOFs have been utilized in a wide range of applications such as gas separation, storage, adsorption, catalysis, drug delivery, other therapeutic purposes, sensors, materials for electrodes, carriers, and membranes.[1–5] Among a large number of MOFs, zirconium-based MOFs (Zr-MOFs) stand out with significant advantages. These MOFs not only originate from abundant and inexpensive metal sources but also possess superior chemical stability and show excellent activity in adsorptive and catalytic applications, especially for ion trapping thanks to the existence of Zr-nodes with great ionic affinity.[6–8]

One of the recent concepts to enhance the performance of Zr-MOFs is defect engineering, in which structural disorders have been reported to be decisive in improving their properties and functions.[9–12] These defect-induced active sites, along with high porosity, make defective Zr-MOFs an ideal candidate for decontaminating applications such as dealing with chemical warfare agents, adsorbing organic dyes, organo-arsenic compounds, and gas pollutants.[13–18] Amino-modified Zr-MOFs, UiO-66-D-NH_2 (UiO = Universitetet i Oslo), were effectively applied to remove low-concentration oxo-arsenic species in water. The combination of defect generation with amino modification provided more Zr-OH active sites and promoted the formation of As–O–Zr coordination, which led to enhanced adsorption behavior of UiO-66-D-NH_2 in simulated wastewater, with the adsorption affinity 3.8 times higher than that of original UiO-66.[13] Clark *et al.* reported highly defective UiO-66 materials by varying the amount of concentrated HCl in solvothermal synthesis. This series of Zr-MOFs exhibited substantial adsorption capacities and fast adsorption rates to contaminants due to the increase in not only pore sizes and internal surface but also coordinatively unsaturated Zr sites that can bind to the guest sulfonate groups. They also showed high selectivity for perfluorooctane

[a] *Department of Chemical Engineering, Ho Chi Minh City University of Technology (HCMUT), 268 Ly Thuong Kiet street, District 10, Ho Chi Minh City, 70000, Vietnam. E-mail: lvha@hcmut.edu.vn*
[b] *Vietnam National University Ho Chi Minh city, Linh Trung Ward, Ho Chi Minh City, 70000, Vietnam*
[c] *Chemical Engineering, Competence Centre for Catalysis, Chalmers University of Technology, Gothenburg, SE-412 96, Sweden. E-mail: phuoc@chalmers.se*

† Electronic supplementary information (ESI) available. See DOI: https://doi.org/10.1039/d2nj05693c

sulfonate (n-$C_8HF_{17}O_3S$) in the presence of competitive anionic species such as Cl^-, SO_4^{2-}, and Cr (VI).[14]

While UiO-66 with coordinatively saturated Zr-clusters is probably the most common Zr-MOF engaged in the defect engineering approach, both through *de novo* synthesis and post-synthetic treatment,[19–24] the performance of Zr-MOFs may still be further improved by reducing their connectivity. In fact, MOF-808, a representative 6-connected Zr-MOF based on a trimesate ligand (1,3,5-benzenetricarboxylate), could be considered a more promising candidate than the Zr-MOFs built with 12-connected zirconium clusters due to the inherent active centers generated by the modulated synthesis approach.[25–27] To the best of our knowledge, although there have been several studies on MOF-808 with deliberated introduced defects, most of them aimed for water adsorption, phosphate sequestration, and catalytic applications,[12,25,27–30] while the employment of defective MOF-808 for the removal of contaminants in aqueous solution is still rare in the literature.[31,32] Recently, original MOF-808 turned out to be an effective adsorbent to capture organic dyes and oxometallate compounds, namely sunset yellow, quinoline yellow, and the Cr (VI) anion, with impressive performances as compared to traditional materials, such as activated carbon or mesoporous silica materials.[26] Although this finding provided a comprehensive overview regarding the impact of the MOF-808 morphology, including particle size and crystallinity on its anion trapping ability, the effect of defective sites, which could also serve as effective active centers, was not mentioned. In fact, introducing additional defects on MOFs constructed with trimesate linkers, such as Cu- and Ru-MOFs, could be simply conducted by the mixed-linker approach.[33,34] In this work, a ditopic ligand (5-hydroxyisophthalic acid or 5-aminoisophthalic acid) was used to partially replace the original tritopic ligand (1,3,5-benzenetricarboxylic acid) in the construction of MOF-808 under hydrothermal conditions. The additional appearance of adsorptive sites resulted in a significant improvement in the adsorption performance of MOF-808 for various organic dyes and Cr (VI) anionic species, which might encourage further research on its application for water treatment.

Experimental section

Materials and instrumentation

All reagents and starting materials, including zirconium (IV) oxychloride octahydrate ($ZrOCl_2{\cdot}8H_2O$ – 97.0%), 1,3,5-benzenetricarboxylic acid (H_3BTC – 98.0%), 5-aminoisophthalic acid (H_2BTC-NH_2 – 94.0%), 5-hydroxylisophthalic acid (H_2BTC-OH – 97.0%), deuterium chloride (DCl – 99.0 atom% D), cesium fluoride (CsF – 99.0%), potassium dichromate ($K_2Cr_2O_7$ – 99.5%), quinoline yellow ($C_{18}H_9NNa_2O_8S_2$ – 95.0%), sunset yellow ($C_{16}H_{10}N_2Na_2O_7S_2$ – 90.0%), methyl orange ($C_{14}H_{14}N_3NaO_3S$ – 85.0%), malachite green ($C_{23}H_{25}ClN_2$ – 90.0%), and methylene blue trihydrate ($C_{16}H_{24}ClN_3O_3S$ – 90.0%), were purchased from commercial suppliers (Sigma-Aldrich, Acros Organics, and Fisher Scientific). They were used as received without further purification.

Synthesis of MOF-808 analogues. In a typical procedure for the synthesis of pristine MOF-808, $ZrOCl_2{\cdot}8H_2O$ (0.81 g, 2.51 mmol) and H_3BTC (0.18 g, 0.86 mmol) were dissolved separately using 75 mL of a mixture of DMF and formic acid (1 : 1 v/v) in total.[26] The obtained solutions were then mixed and heated in an oven at 80 °C for 72 h. After cooling to room temperature, the solid was collected and washed with DMF (30 mL × 3) and acetone (30 mL × 3). The solid product was then dried under vacuum at 120 °C for 5 h.

The synthesis of defective MOF-808 followed the same protocol as the synthesis of MOF-808 but used a mixture of linkers. In detail, 25 mol% of the total amount of H_3BTC was replaced by H_2BTC-NH_2 (0.0388 g, 0.215 mmol) or H_2BTC-OH (0.0391 g, 0.215 mmol). The resulting materials were henceforth denoted as MOF-808-NH_2 and MOF-808-OH, respectively.

Characterization of MOF-808 analogues. Powder X-ray diffraction (PXRD) patterns were recorded using a D8 Advance Bruker powder diffractometer with Cu-Kα_1 radiation (λ = 1.5418 Å). The instrument was equipped with a Ni filter and was operated at 40 kV and 40 mA. The measurements were performed at room temperature in the scanning range of 2θ = 2–30°, at a step size of 0.01°, and a scan rate of 0.60° per minute. The crystallite size (τ) and cell parameter (a) were calculated for five main reflections (111), (311), (222), (400), and (331) from the XRD patterns using eqn (1) and (2), respectively.[35] The input information on the diffraction angle (2θ) and full width at half maximum (FWHM) of each peak was derived from single peak fitting mode using FullProf software.

$$\tau = \frac{0.9\lambda}{\beta \cos\theta} \tag{1}$$

$$a = \frac{\lambda}{2 \sin \theta}\sqrt{h^2 + k^2 + l^2} \quad \text{(Cubic structure)} \tag{2}$$

where λ is the X-ray wavelength, β is the FWHM, θ is the Bragg angle, and (hkl) are the Miller indices of planes.

Morphology of the samples was analyzed by field emission scanning electron microscopy (FESEM) using a Hitachi SU 8010 microscope with the magnification ranging from ×5000 to ×20 000 at an accelerating voltage of 10 kV. The average particle size was determined by measuring the sizes of more than 100 particles using ImageJ software.

Nitrogen physisorption measurements were carried out on a Micromeritics ASAP 2020 volumetric adsorption analyzer system. The samples were activated at 150 °C under vacuum for 5 h before the adsorption/desorption isotherm was measured at 77 K using a high-purity nitrogen gas. Surface areas calculated using the Brunauer–Emmett–Teller (BET) model were determined within a relative pressure range of 0.01–0.10 p/p°. The pore size distribution was assessed using the density functional theory (DFT) method.

Thermogravimetric analysis (TGA) was investigated using a Mettler Toledo TGA/DSC Star^e System interfaced with a PC using Star^e software. In each experiment, the sample was loaded in an alumina pan and heated at a rate of 5 °C min^{-1} from 30 °C to 850 °C under air flow.

For proton nuclear magnetic resonance (^{1}H-NMR) studies, the activated samples were digested in 5 drops of deuterated hydrochloric acid (DCl, 20%) with 15 mg of CsF in 6 h. Deuterated DMSO (DMSO-d_6) was added to the obtained solution prior to measurement. A Bruker spectrometer was employed to record ^{1}H-NMR spectra at 600 MHz. Chemical shifts (ppm) were referenced to tetramethyl silane (0.00 ppm).

A Thermo Scientific G10S UV-Vis device was utilized to measure UV-Vis absorbance. The concentration of $K_2Cr_2O_7$ and the dye solution was determined based on the calibration curves which depicted the relationship between the concentration and the corresponding absorbance recorded at its wavelength of maximum absorbance. It was noted that the adjustment of pH to approx. the initial value was conducted prior to UV-Vis measurement.

Adsorption studies

$Cr_2O_7^{2-}$ adsorption. $K_2Cr_2O_7$ adsorption experiments were conducted under ambient conditions in an aqueous phase. In a typical procedure, 10 mg of activated MOF-808 was added into 15 mL of the $K_2Cr_2O_7$ solution with a concentration of 500 ppm (500 mg of $K_2Cr_2O_7$/L, pH $\sim$ 4.6). The obtained mixture was then stirred at 1000 rpm for 120 min at room temperature. After adsorption, the solid material was separated by centrifugation (3000 rpm for 30 min).

The concentration of $K_2Cr_2O_7$ after the adsorption was determined based on the calibration curve which was established from a linear regression of the concentration *versus* its corresponding absorbance at 351 nm. The adsorption capacity (mg g^{-1}) was calculated based on a decrease in the $K_2Cr_2O_7$ concentration after the adsorption. Because the pH-dependent equilibrium of $Cr_2O_7^{2-}/CrO_4^{2-}$ could immensely affect the UV-Vis spectrophotometric result, the pH value of post-adsorbed solutions was adjusted to a pH of $\sim$ 4.6 using diluted acetic acid or ammonia solutions prior to UV-Vis absorbance measurements.

Dyes adsorption. Zr-MOFs were used for the adsorptive removal of both anionic and cationic dyes. The anionic dyes included quinoline yellow, sunset yellow, and methyl orange while the cationic dyes were methylene blue and malachite green. The dye adsorption experiments were carried out similarly for the study of $K_2Cr_2O_7$, in which 10 mg of activated MOF-808 was added into 15 mL of the 500 ppm solution of a single dye. The resulting mixture was subsequently stirred for 120 min under ambient conditions. The pH of the clear dye solution, obtained after the removal of solid materials by centrifugation, was adjusted with diluted acetic acid or ammonia solution to eliminate the effect of pH on the UV-Vis absorbance results. The wavelength of maximum absorbance for each dye is presented in Table S1 (ESI†).

For comparison purposes, the adsorption experiments of dyes and $Cr_2O_7^{2-}$ were also performed on UiO-66, SBA-15, and activated carbon (AC). UiO-66 was synthesized by the protocol reported by Cirujano and Xamen.[19] SBA-15 was synthesized as reported elsewhere.[36] Activated carbon was purchased from Sigma Aldrich. The specific surface area was 908 m^2 g^{-1} for UiO-66, 1120 m^2 g^{-1} for SBA-15, and 1050 m^2 g^{-1} for AC.

Adsorption kinetics. Two models, namely pseudo-first-order and pseudo-second-order (eqn (3) and (4)) formula, were also employed to investigate the kinetic models of adsorption that occurred onto defective MOF-808 structures:[37]

$$\ln(Q_e - Q_t) = \ln Q_e - k_1 \times t \quad (3)$$

$$\frac{t}{Q_t} = \frac{t}{k_2} \times \frac{1}{Q_t^2} + \frac{1}{Q_e} t \quad (4)$$

in which Q_e is the adsorption capacity at equilibrium (mg g^{-1}), Q_t is the adsorption capacity at an interval time t (mg g^{-1}), and k_1 and k_2 are the rate constants (L min^{-1}).[37]

Besides, the adsorption mechanism of adsorbates that took place onto the surface structure of the defective MOF-808 was also studied by utilizing the Langmuir and Freundlich adsorption isotherm models (eqn (5) and (6)):[38]

$$\frac{C_e}{Q_e} = \frac{1}{K_L \times Q} + \frac{C_e}{Q_o} \quad (5)$$

$$\ln Q_e = \frac{1}{n} \ln C_e + \ln K_F \quad (6)$$

in which Q_e is the adsorption capacity at equilibrium (mg g^{-1}), C_e is the equilibrium concentration in solution (mg L^{-1}), and Q_o is the maximum amount of adsorption (mg g^{-1}). The K_L and K_F values are Langmuir and Freundlich constants, related to the energy of adsorption.[38]

Recycling test. For the recycling test, the defective MOF-808 adsorbent was separated by centrifugation from an aqueous solution. The collected material was then washed five times with dimethylformamide (DMF) and acetone containing 2 wt% of HCl to remove adsorbates and re-drying under vacuum conditions at 105 °C for 4 h. The activated materials were then reused for the next adsorption experiment.

Results and discussion

Material synthesis and characterization

In this work, defective MOF-808, including MOF-808-OH and MOF-808-NH_2, were synthesized by the solvothermal method.[26,39] The reaction of $ZrOCl_2{\cdot}8H_2O$ and organic building blocks (H_3BTC and H_2BTC-OH/H_2BTC-NH_2) proceeded at 80 °C for 72 h (Fig. 1). This procedure was slightly modified from the previous reports,[39–41] which employed a higher temperature of 120 °C for 24 h. The experiments at a lower temperature with a prolonged reaction time were selected to promote the selective formation of highly crystalline Zr-MOFs and facilitate the access of guest linkers into the MOF-808 structure to form crystals containing expected defects of the missing linkers.[42,43]

Fig. 2 presents the PXRD patterns of pristine MOF-808 and defective MOF-808. The most intensive peak at 2θ = 4.35° observed for MOF-808 was indexed to the (111) plane of the octahedral crystal, while two other reflections at 2θ = 8.33° and 8.70° were assigned to the (311) and (222) planes, respectively.[39,44] It is noted that the narrow width and high

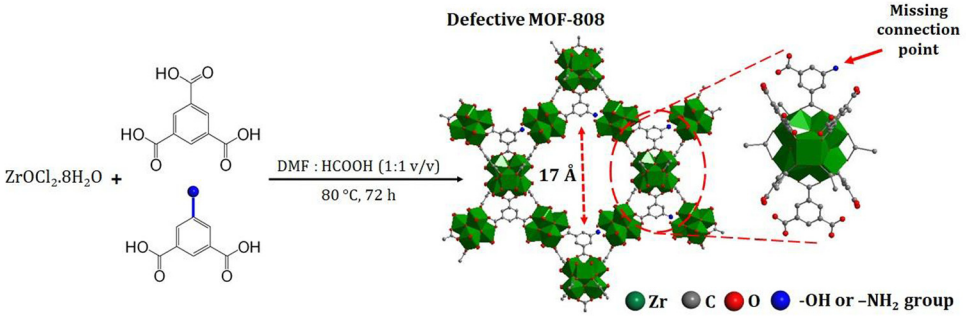

Fig. 1 Synthesis of defective MOF-808-OH and MOF-808-NH_2.

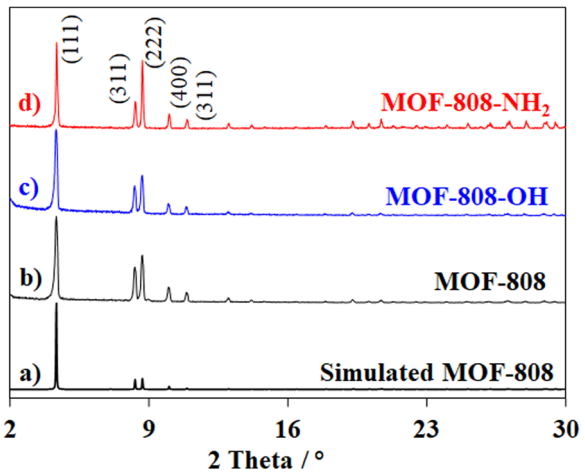

Fig. 2 PXRD patterns of simulated MOF-808 (a), pristine MOF-808 (b), MOF-808-OH (c), and MOF-808-NH_2 (d).

intensity of the reflections indicated the disciplined arrangement of crystal planes, resulting in a high degree of crystallinity.[45] The PXRD patterns of both MOF-808-OH and MOF-808-NH_2 were similar to that of pristine MOF-808, suggesting that the presence of asymmetric linkers did not significantly affect the molecular geometry of MOF-808-OH and MOF-808-NH_2 crystals. However, a modest drop in the relative intensity of some diffraction peaks in their pattern compared to the original MOF-808 phase indicated the loss of crystallinity, which could be derived from the formation of missing defect sites in the frameworks.[46] In more detail, standard MOF-808 had a lattice parameter of the unit cell of around 35.36 ± 0.02 Å which was close to the values reported in the literature.[39,44] MOF-808-OH showed similar cell parameters to MOF-808 while MOF-808-NH_2 exhibited a smaller size of unit cell (35.27 ± 0.06 Å). A slight contraction of the lattice parameter increased the crystal size of MOF-808-NH_2 by 35% compared to bare MOF-808 (Table 1).

Fig. 3 shows the SEM images of pristine MOF-808 and its analogues. As expected, no remarkable differences were observed between the defective and original materials. They all indeed showed well-shaped octahedral crystals, which was in good agreement with the previous reports.[25,26,39] These high-quality crystals were obtained as a result of employing formic acid as a modulator, which would compete with organic building blocks, thereby slowing down the reaction rate and nucleation process, and supporting the self-repair of the network.[24,47,48] Besides, defect inducers, including 5-hydroxyisophthalic acid or 5-aminoisophthalic acid, could also act as additional modulators since they were ditopic linkers containing only two carboxylic acid groups instead of three connecting points as 1,3,5-tricarboxylic acids.[49–51] Consequently, the particles of MOF-808-OH and MOF-808-NH_2 could be facilitated to reach the size of approximately 800 nm, slightly bigger than that of pristine MOF-808 with a size of about 600 nm under the same synthesis conditions. A significant difference in the size of crystals calculated from the XRD data using the Scherrer equation and the particle size recorded from SEM pictures implied the imperfection of MOF-808 crystals, which could be derived from the formation of defective sites in their structure.[52,53]

^{1}H-NMR (proton nuclear magnetic resonance) analysis has been considered as a powerful technique to confirm the presence of missing linkers in the structure of MOF-808 because of a significant difference in the spectral characteristics of the primary linker (1,3,5-tricarboxylate, BTC) in pristine MOF-808 and the two secondary linkers, namely, 5-hydroxyisophthalate (BTC-OH) or 5-aminoisophthalate (BTC-NH_2).[12,41] Moreover, the

Table 1 Physical properties of MOF-808 and defective MOF-808 materials

Sample name	Cell parameter[a] (Å)	Crystal size[a] (nm)	BET surface area (m^2 g^{-1})	Average pore diameter[b] (Å)	V total pore volume[b] (cm^3 g^{-1})
MOF-808	35.36 ± 0.02	65 ± 2	1910	15.0	0.76
MOF-808-OH	35.40 ± 0.01	66 ± 3	2611	17.0	0.87
MOF-808-NH_2	35.27 ± 0.06	88 ± 6	3085	17.0	0.95

[a] Cell parameters were calculated from XRD analysis. [b] Average pore diameter and pore volume were calculated from N_2 physisorption data using the DFT method.

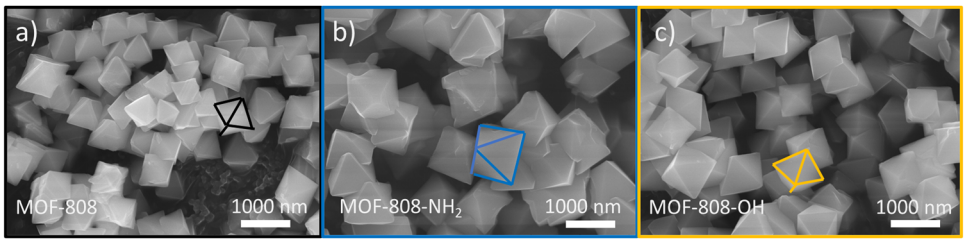

Fig. 3 SEM images of pristine MOF-808 (a), MOF-808-OH (b), and MOF-808-NH_2 (c).

^{1}H-NMR method also allowed quantifying the ratio of defective linkers in the MOF structure. The ^{1}H-NMR spectrum of pristine MOF-808 showed three chemical shifts at 8.54 ppm, 8.09 ppm, and 7.86 ppm, which were assigned to the non-acidic protons in 1,3,5-tricarboxylate, formic acid, and dimethylformamide (–CHO), respectively (Fig. 4).[51,54] On the other hand, the ^{1}H-NMR spectrum of MOF-808-OH showed the additional appearance of two proton signals at 7.51 ppm and 7.92 ppm, corresponding to three aromatic protons of asymmetric BTC-OH linkers. Although these peaks slightly shifted to higher chemical shifts compared to the NMR spectrum of the original BTC-OH linker (from 7.92 ppm to 7.87 ppm and 7.51 ppm to 7.50 ppm), the integration ratios remained approximately 1 : 2, which matched with two equivalent protons out of three.[51] The amount of mixed linkers incorporated into MOF-808-OH was then calculated to be around 7% mol of the total amount of two linkers based on ^{1}H NMR signal integration of the characteristic peaks of BTC and BTC-OH. Consequently, the formula of MOF-808-OH could be considered as $[Zr_6O_4(OH)_4(BTC)_{1.866}(BTC\text{-}OH)_{0.134}(HCOO)_6]$. Similarly, the ^{1}H NMR spectrum of MOF-808-NH_2 shows two additional proton peaks at 7.89 and 8.25 ppm, which were characteristic of the aromatic protons in the 5-aminoisophthalate moiety. This organic building block accounted for about 3% of the total molar amount of linkers in the MOF-808-NH_2 structure, and the molecular formula of MOF-808-NH_2 was determined to be $Zr_6O_4(OH)_4(BTC)_{1.9478}(BTC\text{-}NH_2)_{0.05825}(HCOO)_6$.

However, no significant changes were observed between the thermogravimetric analysis (TGA) profiles of MOF-808 and MOF-808-OH/MOF-808-NH_2 (Fig. S1, ESI†). This could be because the percentages of the secondary linkers are small (7 and 3%) and the molecular weights of the three linkers were also quite similar, which led to no difference in the weight loss from the TGA measurements. The generated defect percentage was much lower than the used number of defective linkers. Even a significant increase in the amount of defect inducers up to 50 mol% did not generate more defects, which was confirmed by the NMR spectrum (Fig. S2, ESI†). This might be because the number of defects, which could be additionally introduced into MOF-808, was limited by its stable structural nature. It should be noted that MOF-808 with 8-connected Zr-clusters could be also considered as a defective structure of the idealized 12-connected Zr-MOFs. Generating additional defects by employing bidentate ligands instead of tritopic linkers could decrease the quantity of the "struts" in their structure and MOF-808 would be more vulnerable.[12,55]

Infrared spectroscopy (IR) was also employed to clarify the presence of the functional groups of the defect inducers in MOF-808 (Fig. 5). The FT-IR spectrum of pristine MOF-808 exhibited three intensive bands at approximately 1606, 1380, and 650 cm^{-1}, which respectively corresponded to the carbonyl vibrations (asymmetric and symmetric stretching) and Zr–O–Zr bonds.[39] These characteristic vibrations were also present in the spectra of both defective MOF-808. Moreover, two additional weak IR signals at 3676 and 3292 cm^{-1} were observed in the spectra of MOF-808-OH and MOF-808-NH_2, respectively. The former was assigned to the phenolic –OH stretching vibration,[56,57] while the latter was ascribed to the free N–H stretching of amino groups.[58] These vibrations belonged to the functional groups of the BTC-OH and BTC-NH_2 linkers and therefore it confirmed the successful incorporation of these secondary linkers in the structure of defective MOF-808.

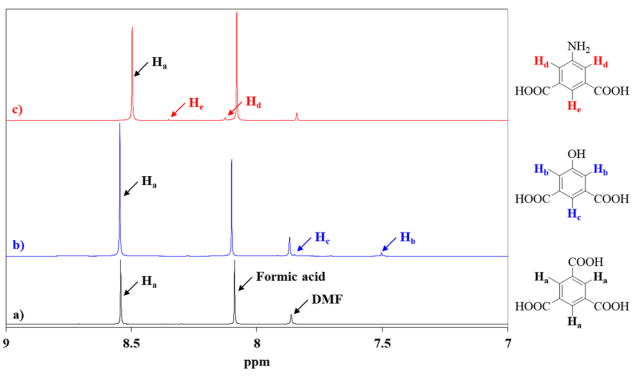

Fig. 4 NMR spectra of MOF-808 analogues.

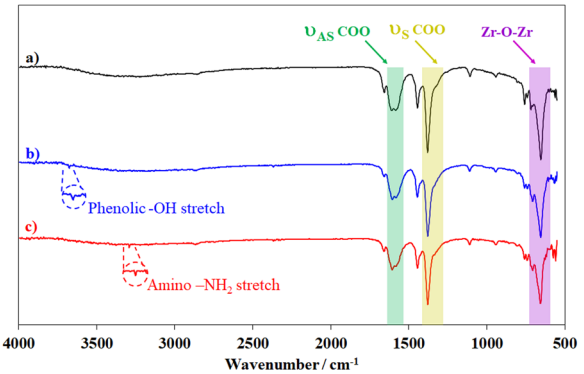

Fig. 5 FT-IR spectra of pristine and defective MOF-808: (a) MOF-808, (b) MOF-808-OH, and (c) MOF-808-NH_2.

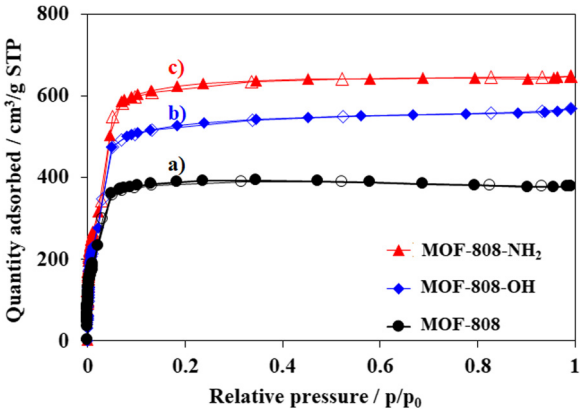

Fig. 6 Adsorption behavior of MOF-808 (a), MOF-808-NH_2 (b) and MOF-808-OH (c).

The nitrogen physisorption isotherms of pristine MOF-808 and modified MOF-808 showed typical type I of the IUPAC classification with no further N_2 adsorption at $p/p_0 > 0.1$, indicating that the highly microporous structure of MOF-808 was maintained.[39] However, the presence of defective sites induced a significant increase in nitrogen uptake. Indeed, the specific surface areas of MOF-808-OH and MOF-808-NH_2 were found to be 2611 and 3085 $m^2\ g^{-1}$, respectively, which increased by 36–62% as compared to the value of pristine MOF-808 (1910 $m^2\ g^{-1}$) (Fig. 6). The partial substitution of the standard linker with asymmetric ones could boost the pore volume and surface area. As mentioned in recent reports, the formation of defective sites caused by defect inducers such as modulators or asymmetric linkers in the framework could expand inherent pores.[46,59,60] This proposal was supported by the pore size distribution result. The average pore size of MOF-808 was around 15 Å while the pore of defective MOFs was slightly increased to 17 Å for both MOF-808-OH and MOF-808-NH_2 (Fig. 7). Moreover, the total pore volume of both defective MOFs was 0.9 $cm^3\ g^{-1}$, increasing by approximately 18% compared to that of MOF-808. The increments in both pore size and total pore volume of porous materials provide more accessible storage spaces which would subsequently induce a significant increase

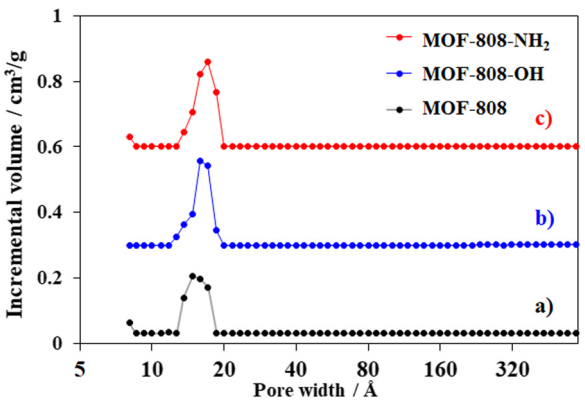

Fig. 7 The pore size distribution of MOF-808 (a), MOF-808-NH_2 (b) and MOF-808-OH (c).

in trapping guest molecules.[61] Therefore, it is expected that MOF-808 having defect sites would be an efficient adsorbent for removing organic dyes from an aqueous solution.

Adsorption studies. Aside from the improvement in accessible pore spaces, the nature of adsorptive sites, *e.g.* functional groups or charged sites in frameworks, was also a key factor impacting the adsorption capacity of porous materials.[62] In the case of Zr-MOFs, the acidic centers derived from coordinatively unsaturated zirconium clusters acted as efficient active sites in various applications.[62,63] However, it was difficult to find these open centers in the well-known 12-connected Zr-MOFs, such as the UiO-66 family.[20] Therefore, introducing additional defects in Zr-MOFs with reduced Zr-cluster connectivity might offer as many acidic centers as possible, which could significantly improve the catalytic activity of the host materials.[50,51] The addition of these acidic active sites could also upgrade the removal performance for anionic contaminants, such as organic dyes and oxometallic compounds. To take advantage of the effectiveness of these active centers in MOF-808-OH and MOF-808-NH_2, a series of adsorption experiments were investigated towards removing anionic dyes (quinoline yellow, sunset yellow, methyl orange), cationic dyes (malachite green, methylene blue) and an oxometallate ($K_2Cr_2O_7$) (Fig. 8 and Table S1, ESI†).

The effects of time (0–300 min) and initial concentration (0–1500 ppm) on the trapping capacity of MOF-808-OH and MOF-808-NH_2 were investigated. As shown in Fig. 9a and b, the ion adsorption of both defective Zr-MOFs proceeded rapidly in the first 30 min, and then slowed down gradually before reaching a plateau after about 60 min. No further improvements in the adsorption capacity were observed over a prolonged time. It was found that the trapping capacity of both materials for each dye was similar and the uptakes for anions were considerably higher as compared with cationic dyes. Specifically, the anion species capturing capacity of MOF-808-OH could reach up to 633 mg g^{-1} for sunset yellow, 702 mg g^{-1} for quinoline yellow, 714 mg g^{-1} for methyl orange, and 164 mg g^{-1} for the chromium (VI) anion, while the values for cationic dyes were 291 mg g^{-1} for malachite green and 217 mg g^{-1} for methylene blue (Fig. 9a). The adsorption capacity of MOF-808 for organic anions was about four-fold higher than that of the inorganic chromium (VI) anion. This might be related to the larger size of the organic anion than the inorganic one, which perhaps enhanced the confinement of the former in the pore of MOF-808-OH. Besides, the defective materials clearly showed impressive performances towards removing anionic species *versus* cationic ones, in which the adsorption capacity for organic anions was about 3-fold higher than that for organic cations. This could be rationalized that the additional appearance of acidic sites significantly improved the affinity between MOF-808 and negatively charged ions, subsequently inducing high capturing capacities. A similar adsorption trend was observed for MOF-808-NH_2, in which the adsorption performance for anion dyes was also higher than that for cationic species. The uptake values for sunset yellow, quinoline yellow, methyl orange, chromium (VI) anion,

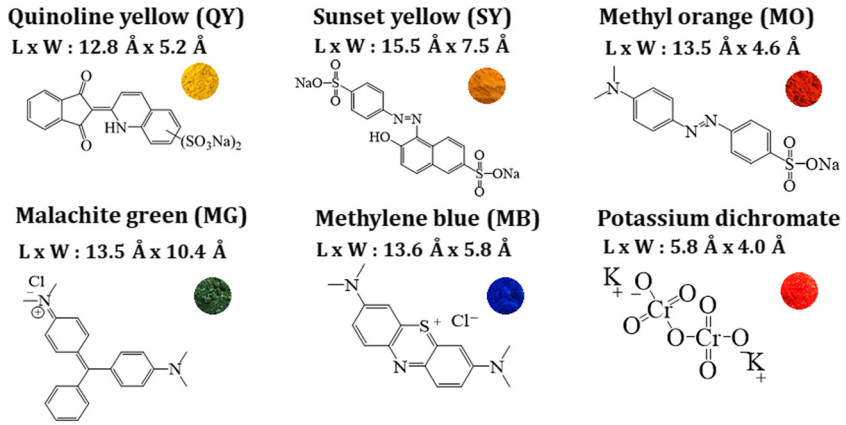

Fig. 8 Chemical formulas of organic dyes and potassium dichromate. The size of organic dyes (length x width) estimated by the materials studio program.

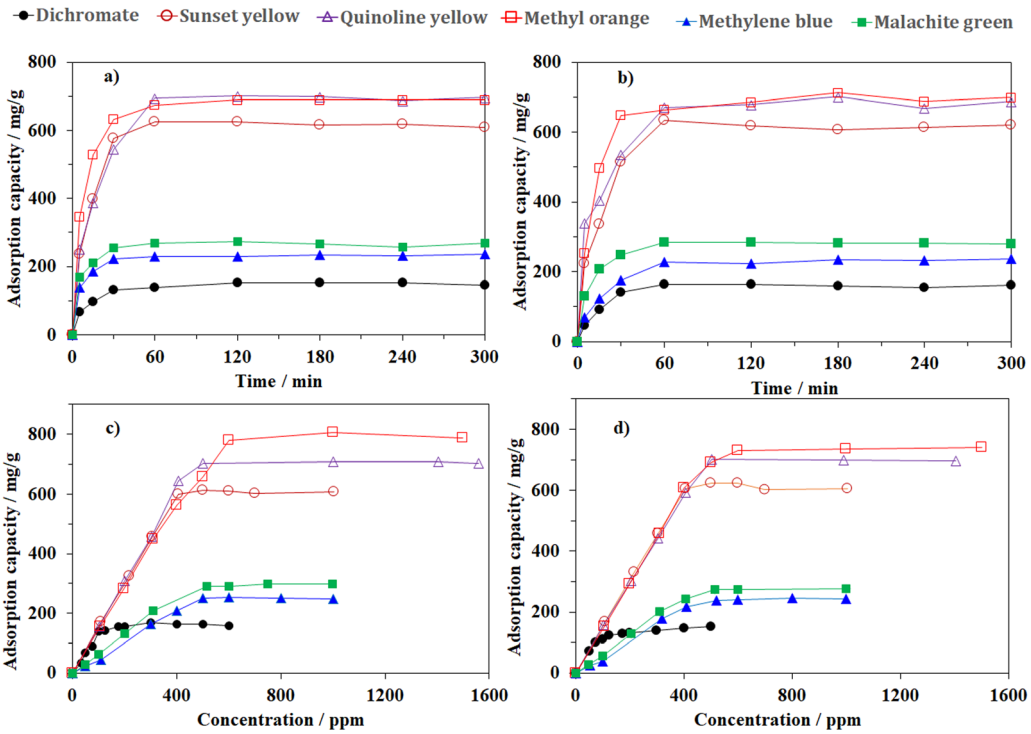

Fig. 9 Effect of the adsorption time and initial concentration of adsorbates on the adsorption capacity of MOF-808-OH (a and c) and MOF-808-NH_2 (b and d).

malachite green, and methylene blue were 626, 702, 690, 153, 273, and 208 mg g^{-1}, respectively (Fig. 9b).

Fig. 9c and d present the equilibrium adsorption capacity of various adsorbates with different initial concentrations on MOF-808-OH and MOF-808-NH_2. In terms of the adsorbate concentration, a similar trend was observed in the trapping capacity of both defective analogues when changing the initial solution. While the removal efficiency gradually decreased as the solution became more concentrated, the adsorption capacity experienced a steady rise until reaching the saturation state (Fig. 9c and d). Specifically, the adsorption capacity of MOF-808-OH could reach up to 170, 613, 708, 805, 249, and 298 mg g^{-1} for chromium (VI) anions (Fig. 9c), sunset yellow, quinoline yellow, methyl orange, methylene blue, and malachite green while the values for MOF-808-NH_2 were 153, 624, 702, 740, 245, and 278 mg g^{-1} (Fig. 9d), respectively. In general, when the initial concentration becomes higher, the ratio of the adsorbate molecules to available adsorption sites increases, resulting in a stronger driving force behind the trapping process.[33] Since the amount of MOFs was kept at 10 mg, the number of active sites was limited. Therefore, once the active centers were occupied and the lack of available sites emerged, the capture process would slow down

and reach a plateau even when the solution concentration was further increased.

To further interpret the adsorption process that occurred in defective MOF-808 structures, the time-dependent adsorption profile was employed based on the pseudo-first-order and -second-order models (eqn (3) and (4)). Generally, the determination coefficients (R^2) were found to be close to 1.00 for the latter and approximately 0.25–0.79 for the former. Moreover, the equilibrium uptake capacity ($Q_{e,cal}$) estimated by the pseudo-second-order model was also closer to the experimental data than those predicted by the pseudo-first-order model (Table 2 and Fig. 10 and Fig. S3–S7, ESI†). Therefore, it would be concluded that the adsorption of both anionic and cationic organic dyes onto the defective MOF-808 structure followed the pseudo-second-order model in which the rate-determining step was involved in both physical and chemical adsorption processes. The trapping capacity of MOFs for organic dyes was found to rely not only on the MOF structure, π–π interactions between the benzene rings of the organic dyes and the aromatic backbones of the ligands, but also on the electrostatic attraction, which would be strongly improved by the presence of positively or negatively charged centers.[5,64,65] Increasing the appearance of defective sites in MOF-808 structures provided more adsorptive sites for capturing anionic organic compounds with higher uptake ($Q_{e,\ cal}$ – mg g^{-1}) and faster adsorption rate constants (g mg^{-1} min^{-1}) than cationic ones (Table 2 and Fig. 10 and Fig. S3–S7, ESI†).

Furthermore, the distribution of adsorbates onto defective Zr-MOF structures was investigated based on the initial concentration-dependent adsorption data *via* utilizing Langmuir and Freundlich models (eqn (5) and (6)). The Langmuir formula describes the process taking place on a uniform surface with one adsorbate molecular layer, while the Freundlich equation refers to reversible adsorption on the heterogeneous surface with the multi-layer distribution of adsorbates.[38,64,66,67] It was found that the isotherm data fit with both the Langmuir and Freundlich models as the determination coefficients were recorded at high values ($R^2 > 0.9$ Table S2 and Fig. 11 and Fig. S8–S12, ESI†). However, the theoretical adsorption capacities of both anionic and cationic compounds based on the Langmuir equation were significantly higher than the experimental ones. It means that this formula was not suitable to describe the interaction between the adsorbates and the adsorptive sites, or the adsorption process was not conducted on a uniform adsorbing surface. The accidental appearance of defect sites in the MOF-808 structures could result in the non-uniformity of adsorptive surfaces with different affinities to adsorbates. The Freundlich model was, therefore, likely more appropriate to describe the adsorption of anionic and cationic compounds onto the defective MOF-808 structures. Besides, the *n* values (Table S2, ESI†) for trapping anions were higher than that of cation adsorption, suggesting that the adsorbing surface was more favorable to the negatively charged ions *versus* the positively charged species.[66] In fact, the missing-linker defects in Zr-MOF structures would lead to the formation of acidic centers which caused a strong pulsive force on cations and thus this decreased the adsorption performance (Fig. 12).

A further experiment was executed to emphasize the introduced defects in removing organic dyes and chromium (VI) anionic species from aqueous solutions. As expected, the removal efficiency of defective MOF-808 compared to the pristine one on all anionic dyes and $K_2Cr_2O_7$ increased by over 30% and almost doubled in the case of quinoline yellow and sunset yellow. This proved that the presence of additional defects in the MOF-808 structure even in low quantities (*e.g.* only 7% and 3% defective sites for MOF-808-OH and MOF-808-NH_2) promoted significantly the adsorption performance (Fig. 13). While these acidic centers led to a decrease in the adsorption performance towards cationic dyes due to the strong pulsive force (Fig. 12). Besides, a change in the pore texture toward enhancing accessible pore spaces due to missing linker defects could contribute to better performance. In particular, linker vacancy defects altered the porosity of the frameworks by enlarging the pore size along with the pore window.[25,41] The pore diameter of defective samples was extended to 17 Å in comparison with 15 Å of standard MOF-808 (Fig. 7). The pore volume was also increased to 0.87 cm^3 g^{-1} for MOF-808-OH and 0.95 cm^3 g^{-1} for MOF-808-NH_2 compared to 0.76 cm^3 g^{-1} for MOF-808. The larger pore diameter with a sparser structure is expected to promote the diffusion process of adsorbates into the pore cavity and facilitate the exposure of active centers.[17] These alterations could be a rational reason for the modest improvement in the removal of cationic dyes, which usually offered weak affinities to acidic positive sites. The capture efficiency of defective MOF-808 was respectively increased to around 5% for malachite green and 20% for methylene blue.

Table 2 Kinetic parameters of pseudo-first-order and -second-order models for the adsorption processes of MOF-808-OH and MOF-808-NH_2

		Pseudo-first-order model						Pseudo-second-order model					
		MOF-808-OH			MOF-808-NH_2			MOF-808-OH			MOF-808-NH_2		
No.	Sample	$Q_{e,cal}$ (mg g^{-1})	$k \times 10^{-2}$ (min^{-1})	R^2	$Q_{e,cal}$ (mg g^{-1})	$k \times 10^{-2}$ (min^{-1})	R^2	$Q_{e,cal}$ (mg g^{-1})	$k \times 10^{-2}$ (g mg^{-1} min^{-1})	R^2	$Q_{e,cal}$ (mg g^{-1})	$k \times 10^{-2}$ (g mg^{-1} min^{-1})	R^2
1	Cr(VI) anion	25.9	8.3	0.296	41.7	6.3	0.521	164.9	0.8	0.998	151.5	1.5	0.998
2	SY	124.8	7.8	0.345	66.6	7.8	0.248	637.4	0.2	0.999	625.7	0.4	0.999
3	QY	171.3	10.5	0.531	126.8	12.1	0.476	704.0	0.2	0.999	718.9	0.2	0.999
4	MO	155.9	9.1	0.559	114.4	11.0	0.685	713.8	0.3	0.999	701.6	0.4	0.999
5	MB	86.6	11.7	0.794	40.1	8.7	0.711	245.5	0.4	0.999	237.6	1.3	0.999
6	MG	45.4	7.5	0.409	29.7	5.9	0.257	284.7	1.0	0.999	266.5	2.3	0.999

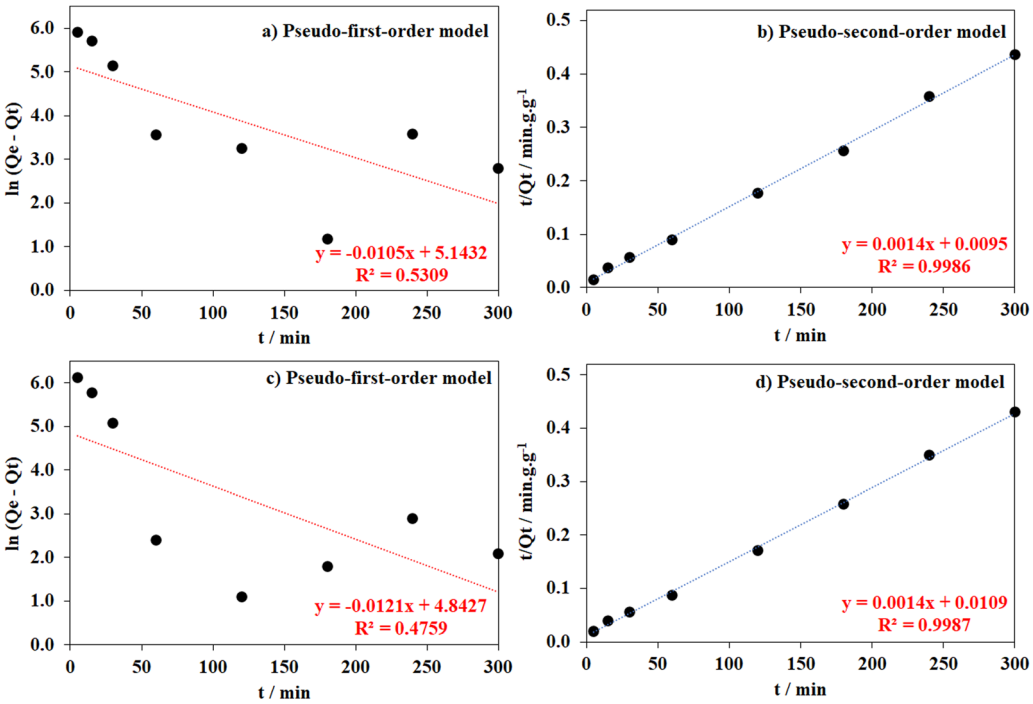

Fig. 10 Pseudo-first-order and -second-order models of quinoline yellow adsorption processes as employing MOF-808-OH (a and b) and MOF-808-NH_2 (c and d).

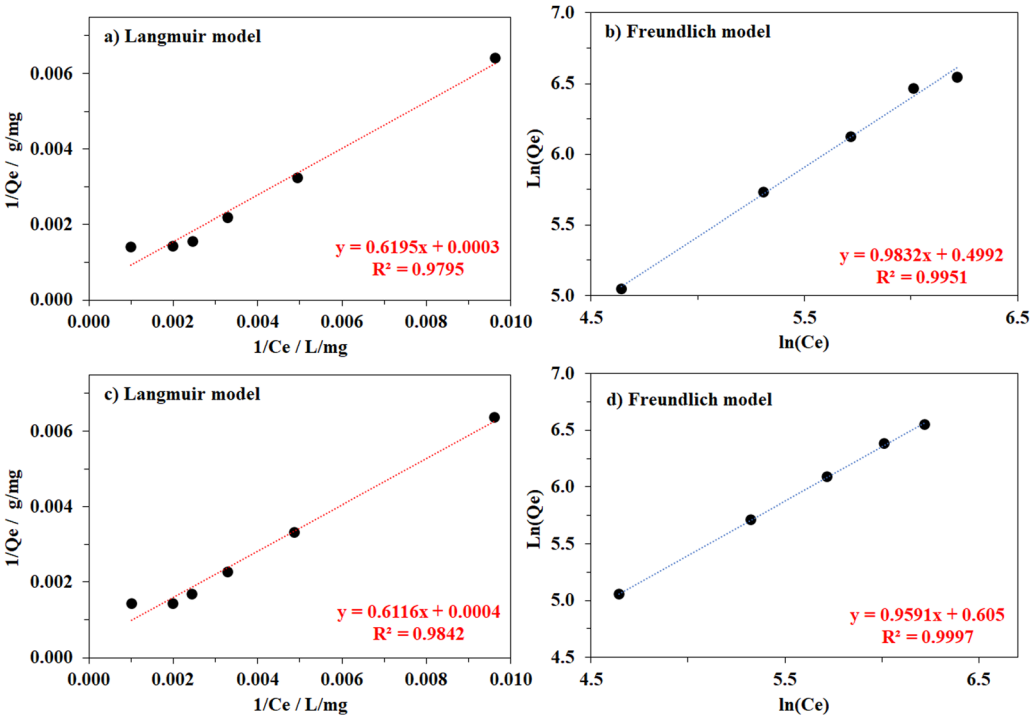

Fig. 11 Quinoline yellow adsorption isotherms of MOF-808-OH (a and b) and MOF-808-NH_2 (c and d) fitting by the Langmuir model and Freundlich model.

Compared to the well-known 12-connected Zr-based MOFs, the capture efficiency for anionic dyes and $Cr_2O_7^{2-}$ of MOF-808 was around 15–40% higher than the results of UiO-66. On the other hand, the abundance of acidic centers in the MOF-808 structure could exhibit a stronger repulsive force to cationic dyes than UiO-66 and result in lower performance for

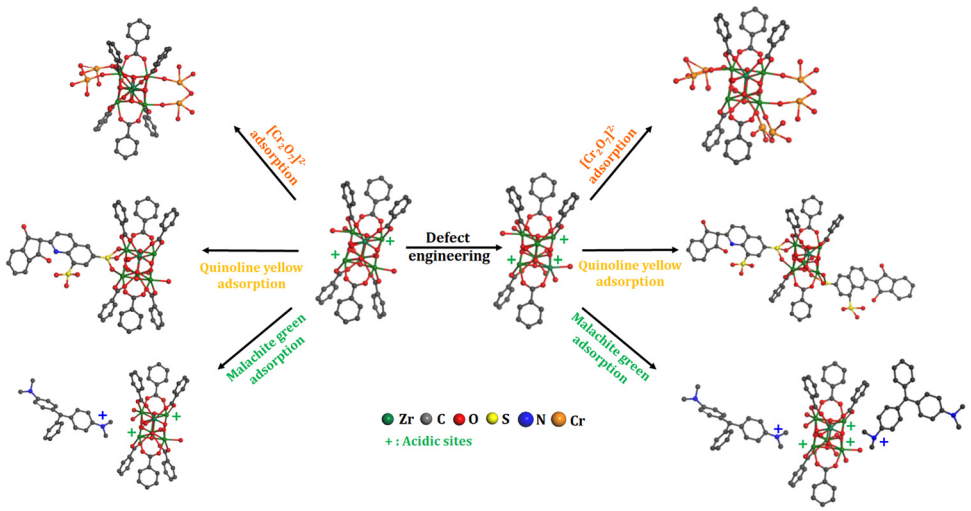

Fig. 12 Plausible model regarding the adsorption of an oxometallate compound ($Cr_2O_7^{2-}$); anionic organic dyes (quinoline yellow); and cationic organic dye (malachite green) in the presence of MOF-808 and its defective structure.

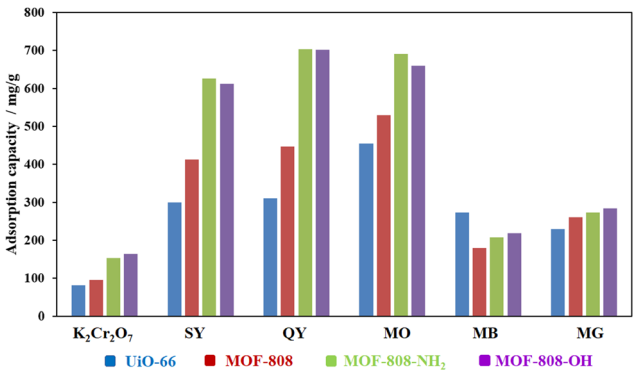

Fig. 13 Comparison of potassium dichromate and dye trapping performance of defective MOF-808 analogues with other adsorbents.

methylene blue (length × width = 13.6 Å × 5.8 Å), which was recorded at 179 mg g^{-1} for MOF-808 and 274 mg g^{-1} for UiO-66. However, with a bulkier molecule such as malachite green (length × width = 13.5 Å × 10.4 Å), the dense structure and small pores in UiO-66 (with an average pore size of 8.6 Å) hindered the adsorption process, resulting in slightly lower capture capacity in comparison with MOF-808 (229 mg g^{-1} for UiO-66 and 260 mg g^{-1} for MOF-808). The formation of strong acidic centers derived from defect sites offered strong electrostatic interactions and boosted the capture efficiency for anionic species.[68]

To gain a deep understanding of the role of additional acidic centers in MOF-808, typical adsorption experiments were carried out by employing two popular adsorbents, including SBA-15 and activated carbon. Both materials have high specific surface areas, namely, 1120 m^2 g^{-1} for SBA-15 and 1050 m^2 g^{-1} for activated carbon. Although the specific area surface of these materials was significantly lower than that of defective MOF-808, their performance for the removal of the cationic dyes was remarkable. Specifically, the trapping capacities of activated carbon for methylene blue and malachite green were 513 and 718 mg g^{-1} (entry 5 in Table 3), respectively, which were around 2.5 times higher than that of defective MOF-808 samples. SBA-15 exhibited lower adsorptive performance than activated carbon, in which the adsorption capacity for methylene blue and malachite green was determined to be 281 and 319 mg g^{-1}, respectively. However, SBA-15 was inactive for the adsorption of anionic dyes and Cr (IV) solutions while the activated carbon showed low uptake for sunset yellow (92 mg g^{-1}), quinoline yellow (95 mg g^{-1}), and methyl orange (86 mg g^{-1}) (entry 6 in Table 3). Also, the adsorption of activated carbon for $K_2Cr_2O_7$ was negligible. A contrast behavior of the adsorption between SBA-15/activated carbon and MOF-808 was likely due to the difference in surface charge. The absence of positively charged centers in SBA-15 and activated carbon structure lowered the repulsive forces towards cationic species,[36,69] and consequently, this improved the removal capacity for cationic dyes. However, the absence of positively charged centers on SBA-15 and activated carbon also

Table 3 Comparison of potassium dichromate and dye trapping performance of defective MOF-808 analogues with other adsorbents. The experiments in this work were carried out in 15 mL of the 500 ppm dye solution in the presence of 10 mg of activated MOF-808

		Adsorption capacity (mg g^{-1})						
No.	Sample	$K_2Cr_2O_7$	SY	QY	MO	MB	MG	Ref.
1	UiO-66	81	299	311	454	274	229	This work
2	MOF-808	96	412	446	529	179	260	This work
3	MOF-808-OH	164	612	701	659	218	284	This work
4	MOF-808-NH_2	153	626	702	690	208	273	This work
5	Activated carbon	0	92	95	86	513	718	This work
6	SBA-15	0	0	0	0	281	319	This work
7	Ui-66-NH_2	34.4	—	—	96.5	29.0	—	70, 71
8	UiO-66-$(OH)_2$	75.5	—	—	—	—	—	70
9	JLU-MOF60	149	—	—	—	—	—	72
10	Cu-MOFs	223	—	—	—	—	—	73
11	MOF-199	—	—	65.4	—	94.4	—	74
12	MIL-101	—	81.3	—	114	—	—	75, 76
13	MOF-235	—	—	—	477	187	—	77

caused a lack of strong adsorption sites, resulting in poor performances for the anionic dyes and $Cr_2O_7^{2-}$ compared to Zr-MOFs.

For the removal of Cr (VI) anions from aqueous solutions, the ideal 12-connected zirconium-based metal–organic frameworks, such as Ui-66 and its relatives, usually exhibited quite modest performances (entries 1, 7 and 8 in Table 3).[70] One popular approach was employing tri- or tetradentate linkers as organic building blocks in designing novel MOFs to further reduce the connectivity of Zr-clusters or increase the number of adsorptive sites. The 4-connected Zr-MOF (JLU-MOF60), which was synthesized from tetradentate pyrazine linkers, is a representative example of when their adsorption capacity for Cr (VI) anions could reach up to 149 mg g^{-1} (entry 9 in Table 3),[72] while this value of the previously functionalized 12-connected Zr-MOFs only remained approximately 80 mg g^{-1}.[70] This strategy could be also applied to other Cu-MOFs for improving their $K_2Cr_2O_7$ trapping capacity. Li and coworkers used a tetracarboxylate linker, namely 1,1′-bis(3,5-dicarboxyphenyl)-4,4′-bipyridinium chlorine, to prepare a novel Cu-MOF, and its trapping capacity could be recorded to be about 223 mg g^{-1} (entry 10 in Table 3).[73] Although employing multidentate linkers offers undeniable benefits in introducing new metal–organic frameworks with ultra-high adsorption capacities, the design and synthesis of such organic building blocks as well as materials have always been a real challenge.[68,78] Therefore, improving the formation of defective sites on typical 8-connected Zr-MOFs, such as MOF-808, by a simplified mixed-linker approach could be suitable for practical applications. Similarly, defective MOF-808 analogues also exhibited impressive performances in comparison with some popular MOFs containing open metal sites, which could serve as adsorptive centers.[55] For instance, MOF-199, a typical metal–organic framework containing open copper centers, could efficiently remove quinoline yellow at 65.4 mg g^{-1},[74] while the capturing capacity of MIL-101 and its composite with graphene oxide with coordinatively unsaturated chrome sites was recorded at approximately 114 mg g^{-1} for methyl orange and 81.3 mg g^{-1} for sunset yellow, respectively (entries 10 and 11 in Table 3).[75,76] MOF-235 containing open iron centers also showed high adsorption capacity for methyl orange of about 477 mg g^{-1} (entry 12 in Table 3). Although these uptake values were generally more impressive than those of the saturated 12-connected UiO-66 and its analogues,[64–66,71,79] they were still significantly lower than the performances of defective 8-connected MOF-808, including MOF-808-OH and MOF-808-NH_2. Obviously, a MOF-808 with a 6-connected Zr-cluster exhibits superior adsorption capacity for anion trapping in an aqueous solution. The additional defect sites in the MOF-808 structure

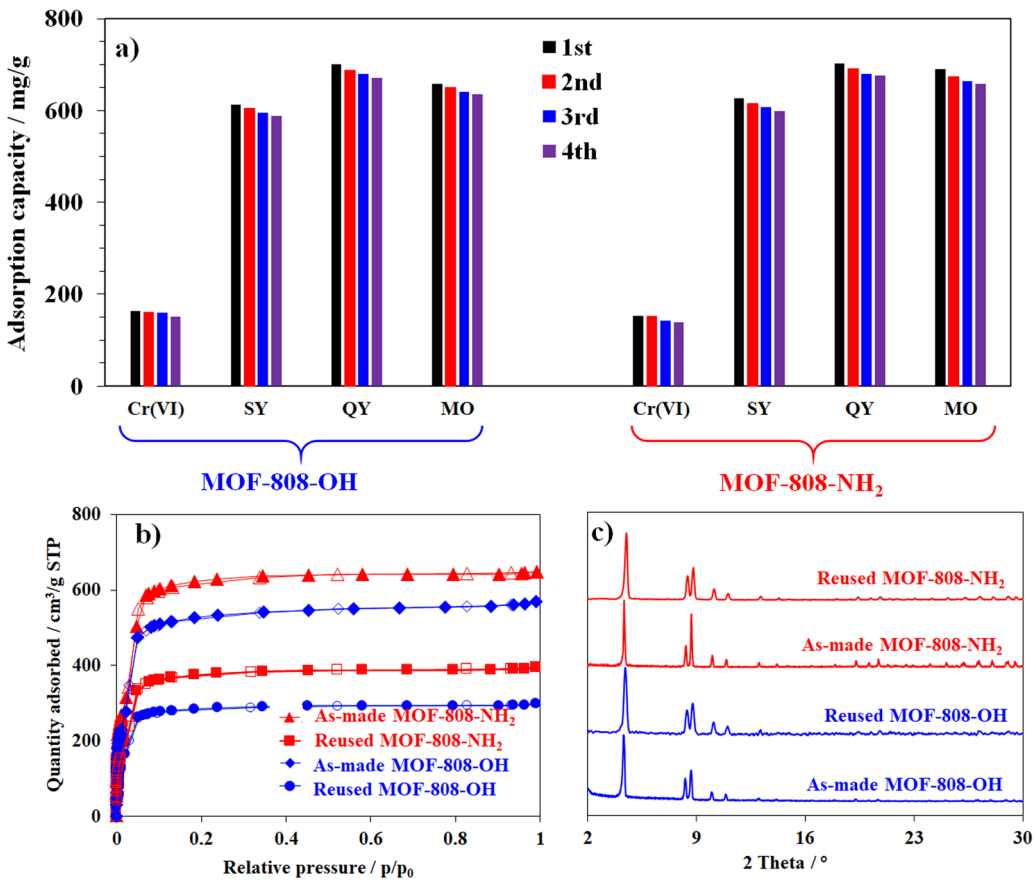

Fig. 14 Recycling test for employing MOF-808-OH and MOF-808-NH_2 in the removal of anionic compounds (a); XRD profiles (b) and nitrogen adsorption behavior (c) of as-prepared defective MOF-808 and defective MOF-808 after three recycling cycles.

played a crucial role since they offered an effective platform for the selective removal of anionic dyes and Cr (IV) in water.

Another key factor for the practical application is the reusability of the absorbents after the adsorption processes.[5,18] In this study, the recycling tests of defective MOF-808 analogues were performed for 4 cycles. After the first run, the MOF-808 adsorbent was separated from the aqueous solution by centrifugation. The collected material was subsequently washed five times with dimethylformamide (DMF) and acetone containing 2 wt% of HCl to remove adsorbates. After that, it was dried under vacuum conditions at 105 °C for 4 h. Activated MOF-808 was consequently employed for the next adsorption cycle. The adsorption capacity of defective MOF-808 materials generally dropped only below approximately 5.0% for anionic organic dyes, while this value for capturing the Cr (VI) anion was 7.9% for MOF-808-OH and 9.2% for MOF-808-NH_2, respectively (Fig. 14a and Table S3, ESI†). However, a significant decrease was observed in the result of nitrogen adsorption at 77 K from approximately 648 $cm^3\ g^{-1}$ to 395 $cm^3\ g^{-1}$ for MOF-808-NH_2 and from 569 to 294 $cm^3\ g^{-1}$ for MOF-808-OH (Fig. 14b). Their BET surface areas were respectively reduced to 1827 $m^2\ g^{-1}$ and 1611 $m^2\ g^{-1}$. This result could be rationalized that the positive centers of the MOF-808 structure could be incompletely regenerated from anionic adsorbates, including $K_2Cr_2O_7$, sunset yellow, quinoline yellow, and methyl orange or a part of acidic sites became inactive after three cycles of the recycling adsorption process due to their strong interactions.[29,65] Besides, the crystallinity of the reused materials only showed a modest decline as the diffraction peaks were broadened in comparison with the respective profiles of the as-prepared defective structures (Fig. 14c). It means that the structures of the defective MOF-808 analogues were stable enough to be recovered and reused at least three times with only a minor decrease in anion trapping.

Conclusions

In this study, the mixed linker method was applied to generate defective sites in the MOF-808 structure, a 6-connected Zr-based MOF with extraordinary adsorption capacity along with excellent stability. The resulting materials contained approximately 3% of mixed linkers in the structure for MOF-808-NH_2 and around 7% for MOF-808-OH. The presence of defects improved the porosity of MOF-808 materials; for example, the specific surface areas were 3085 and 2611 $m^2\ g^{-1}$ for MOF-808-NH_2 and MOF-808-OH, respectively, which were considerably higher than that of standard MOF-808 (1910 $m^2\ g^{-1}$). However, the presence of defects did not alter significantly the molecular geometry, morphology, and thermal stability. Standard MOF-808 and defective MOF-808 were applied for the adsorptive removal of $K_2Cr_2O_7$ and various organic dyes (cationic and anionic). Defective MOF-808 showed remarkable adsorption capacity for anionic dyes. Specifically, defective MOF-808 materials were capable of removing over 80% of anionic dyes, about 20% of $K_2Cr_2O_7$, and around 30% of cationic contaminants in aqueous solution within 2 h of exposure (at an initial adsorbate concentration of 500 ppm) due to the strong affinities between the positive charge of defective MOF-808 towards negatively charged species of the anionic dyes. The advantages of defective MOF-808 as adsorbents were also compared with UiO-66, SBA-15, and activated carbon. The introduction of defects in MOF-808 was a facile and effective strategy to further decrease the connectivity of the unsaturated Zr-cluster and boost the selective removal of anionic contaminants in aqueous solution, showing the great potential of defective materials for wastewater treatment.

Conflicts of interest

The authors declare no competing financial interest.

Acknowledgements

This research was funded by Ho Chi Minh City University of Technology (HCMUT) – VNU-HCM under grant number To-KTHH-2021-12.

References

1 J. D. Evans, B. Garai, H. Reinsch, W. Li, S. Dissegna, V. Bon, I. Senkovska, R. A. Fischer, S. Kaskel, C. Janiak, N. Stock and D. Volkmer, Metal–organic frameworks in Germany: From synthesis to function, *Coord. Chem. Rev.*, 2019, **380**, 378–418.
2 H. Furukawa, E. Cordova Kyle, M. O'Keeffe and M. Yaghi Omar, The Chemistry and Applications of Metal–Organic Frameworks, *Science*, 2013, **341**, 1230444.
3 G. Férey, Hybrid porous solids: past, present, future, *Chem. Soc. Rev.*, 2008, **37**, 191–214.
4 L. Jiao, J. Y. R. Seow, W. S. Skinner, Z. U. Wang and H. L. Jiang, Metal–organic frameworks: Structures and functional applications, *Mater. Today*, 2019, **27**, 43–68.
5 S. H. Goh, H. S. Lau and W. F. Yong, Metal–Organic Frameworks (MOFs)-Based Mixed Matrix Membranes (MMMs) for Gas Separation: A Review on Advanced Materials in Harsh Environmental Applications, *Small*, 2022, **18**, 2107536.
6 S. Yuan, L. Feng, K. Wang, J. Pang, M. Bosch, C. Lollar, Y. Sun, J. Qin, X. Yang, P. Zhang, Q. Wang, L. Zou, Y. Zhang, L. Zhang, Y. Fang, J. Li and H.-C. Zhou, Stable Metal–Organic Frameworks: Design, Synthesis, and Applications, *Adv. Mater.*, 2018, **30**, 1704303.
7 X. Sun, S. Yao, C. Yu, G. Li, C. Liu, Q. Huo and Y. Liu, An ultrastable Zr-MOF for fast capture and highly luminescence detection of $Cr_2O_7^{2-}$ simultaneously in an aqueous phase, *J. Mater. Chem. A*, 2018, **6**, 6363–6369.
8 M. Shahnawaz Khan, M. Khalid and M. Shahid, What triggers dye adsorption by metal organic frameworks? The current perspectives, *Mater. Adv.*, 2020, **1**, 1575–1601.

9 Z. Fang, B. Bueken, D. E. De Vos and R. A. Fischer, Defect-Engineered Metal–Organic Frameworks, *Angew. Chem., Int. Ed.*, 2015, **54**, 7234–7254.
10 J. Canivet, M. Vandichel and D. Farrusseng, Origin of highly active metal–organic framework catalysts: Defects? Defects!, *Dalton Trans.*, 2016, **45**, 4090–4099.
11 S. Dissegna, K. Epp, W. R. Heinz, G. Kieslich and R. A. Fischer, Defective Metal–Organic Frameworks, *Adv. Mater.*, 2018, **30**, 1704501.
12 H. H. Mautschke, F. Drache, I. Senkovska, S. Kaskel and F. X. I. Llabrés Xamena, Catalytic properties of pristine and defect-engineered Zr-MOF-808 metal organic frameworks, *Catal.: Sci. Technol.*, 2018, **8**, 3610–3616.
13 Y. Xu, J. Lv, Y. Song, X. Zhou, C. Tian, X. Hong, Y. Cai, C. Zhao and Z. Lin, Efficient removal of low-concentration organoarsenic by Zr-based metal–organic frameworks: Cooperation of defects and hydrogen bonds, *Environ. Sci.: Nano*, 2019, **6**, 3590–3600.
14 C. A. Clark, K. N. Heck, C. D. Powell and M. S. Wong, Highly Defective UiO-66 Materials for the Adsorptive Removal of Perfluorooctanesulfonate, *ACS Sustainable Chem. Eng.*, 2019, **7**, 6619–6628.
15 H. Y. Zhang, R. H. Shi, H. L. Fan, C. Yang, C. N. Zhang, Y. S. Wang and Z. Tian, Defect creation by benzoic acid in Cu-Based Metal−Organic frameworks for enhancing sulfur capture, *Microporous Mesoporous Mater.*, 2020, **298**, 110070.
16 K. O. Kirlikovali, Z. Chen, T. Islamoglu, J. T. Hupp and O. K. Farha, Zirconium-Based Metal–Organic Frameworks for the Catalytic Hydrolysis of Organophosphorus Nerve Agents, *ACS Appl. Mater. Interfaces*, 2020, **12**, 14702–14720.
17 K. Wang, C. Li, Y. Liang, T. Han, H. Huang, Q. Yang, D. Liu and C. Zhong, Rational construction of defects in a metal–organic framework for highly efficient adsorption and separation of dyes, *Chem. Eng. J.*, 2016, **289**, 486–493.
18 G. T. Tee, X. Y. Gok and W. F. Yong, Adsorption of pollutants in wastewater via biosorbents, nanoparticles and magnetic biosorbents: A review, *Environ. Res.*, 2022, **212**, 113248.
19 F. G. Cirujano and F. X. Llabrés i Xamena, Tuning the Catalytic Properties of UiO-66 Metal–Organic Frameworks: From Lewis to Defect-Induced Brønsted Acidity, *J. Phys. Chem. Lett.*, 2020, **11**, 4879–4890.
20 X. Feng, H. S. Jena, C. Krishnaraj, K. Leus, G. Wang, H. Chen, C. Jia and P. Van Der Voort, Generating Catalytic Sites in UiO-66 through Defect Engineering, *ACS Appl. Mater. Interfaces*, 2021, **13**, 60715–60735.
21 X. Feng, J. Hajek, H. S. Jena, G. Wang, S. K. P. Veerapandian, R. Morent, N. De Geyter, K. Leyssens, A. E. J. Hoffman, V. Meynen, C. Marquez, D. E. De Vos, V. Van Speybroeck, K. Leus and P. Van Der Voort, Engineering a Highly Defective Stable UiO-66 with Tunable Lewis-Brønsted Acidity: The Role of the Hemilabile Linker, *J. Am. Chem. Soc.*, 2020, **142**, 3174–3183.
22 V. V. Butova, A. M. Aboraia, M. Solayman, I. S. Yahia, H. Y. Zahran, A. F. Abd El-Rehim, H. Algarni, G. Khabiri and A. V. Soldatov, The joint effect of naphthalene-system and defects on dye removal by UiO-66 derivatives, *Microporous Mesoporous Mater.*, 2021, **325**, 111314.
23 S. Q. Wang, X. Gu, X. Wang, X. Y. Zhang, X. Y. Dao, X. M. Cheng, J. Ma and W. Y. Sun, Defect-engineering of Zr(IV)-based metal–organic frameworks for regulating CO_2 photoreduction, *Chem. Eng. J.*, 2022, **429**, 132157.
24 I. Abánades Lázaro, C. J. R. Wells and R. S. Forgan, Multivariate Modulation of the Zr MOF UiO-66 for Defect-Controlled Combination Anticancer Drug Delivery, *Angew. Chem., Int. Ed.*, 2020, **59**, 5211–5217.
25 R. Hardian, S. Dissegna, A. Ullrich, P. L. Llewellyn, M.-V. Coulet and R. A. Fischer, Tuning the Properties of MOF-808 via Defect Engineering and Metal Nanoparticle Encapsulation, *Chem. – Eur. J.*, 2021, **27**, 6804–6814.
26 K. D. Nguyen, P. H. Ho, P. D. Vu, T. L. D. Pham, P. Trens, F. Di Renzo, N. T. S. Phan and H. V. Le, Efficient Removal of Chromium(VI) Anionic Species and Dye Anions from Water Using MOF-808 Materials Synthesized with the Assistance of Formic Acid, *Nanomaterials*, 2021, **11**, 1398.
27 C. Simms, F. de Azambuja and T. N. Parac-Vogt, Enhancing the Catalytic Activity of MOF-808 Towards Peptide Bond Hydrolysis through Synthetic Modulations, *Chem. – Eur. J.*, 2021, **27**, 17230–17239.
28 Y. Gu, G. Ye, W. Xu, W. Zhou and Y. Sun, Creation of Active Sites in MOF-808(Zr) by a Facile Route for Oxidative Desulfurization of Model Diesel Oil, *ChemistrySelect*, 2020, **5**, 244–251.
29 Y. Wu, Y. Li, J. Gao and Q. Zhang, Recent advances in vacancy engineering of metal–organic frameworks and their derivatives for electrocatalysis, *SusMat*, 2021, **1**, 66–87.
30 Y. Tao, B. Yang, F. Wang, Y. Yan, X. Hong, H. Xu, M. Xia and F. Wang, Green synthesis of MOF-808 with modulation of particle sizes and defects for efficient phosphate sequestration, *Sep. Purif. Technol.*, 2022, **300**, 121825.
31 L. Han, X. Liu, X. Zhang, M. Li, D. Li, P. Qin, S. Tian, M. Lu and Z. Cai, Preparation of multivariate zirconia metal–organic frameworks for highly efficient adsorption of endocrine disrupting compounds, *J. Hazard. Mater.*, 2022, **424**, 127559.
32 S. Jia, S. Song and X. Zhao, Selective adsorption and separation of dyes from aqueous solution by a zirconium-based porous framework material, *Appl. Organomet. Chem.*, 2021, **35**, e6314.
33 W. Zhang, M. Kauer, O. Halbherr, K. Epp, P. Guo, M. I. Gonzalez, D. J. Xiao, C. Wiktor, F. X. Liabrés i Xamena, C. Wöll, Y. Wang, M. Muhler and R. A. Fischer, Ruthenium Metal–Organic Frameworks with Different Defect Types: Influence on Porosity, Sorption, and Catalytic Properties, *Chem. – Eur. J.*, 2016, **22**, 14297–14307.
34 S. Marx, W. Kleist and A. Baiker, Synthesis, structural properties, and catalytic behavior of Cu-BTC and mixed-linker Cu-BTC-PyDC in the oxidation of benzene derivatives, *J. Catal.*, 2011, **281**, 76–87.
35 U. Holzwarth and N. Gibson, The Scherrer equation versus the 'Debye-Scherrer equation', *Nat. Nanotechnol.*, 2011, **6**, 534.

36 H. V. Le, S. Parishan, A. Sagaltchik, H. Ahi, A. Trunschke, R. Schomäcker and A. Thomas, Stepwise Methane-to-Methanol Conversion on CuO/SBA-15, *Chem. – Eur. J.*, 2018, **24**, 12592–12599.

37 E. D. Revellame, D. L. Fortela, W. Sharp, R. Hernandez and M. E. Zappi, Adsorption kinetic modeling using pseudo-first order and pseudo-second order rate laws: A review, *Cleaner Eng. Technol.*, 2020, **1**, 100032.

38 S. Kalam, S. A. Abu-Khamsin, M. S. Kamal and S. Patil, Surfactant Adsorption Isotherms: A Review, *ACS Omega*, 2021, **6**, 32342–32348.

39 J. Jiang, F. Gándara, Y.-B. Zhang, K. Na, O. M. Yaghi and W. G. Klemperer, Superacidity in Sulfated Metal–Organic Framework-808, *J. Am. Chem. Soc.*, 2014, **136**, 12844–12847.

40 C. Ardila-Suárez, J. Rodríguez-Pereira, V. G. Baldovino-Medrano and G. E. Ramírez-Caballero, An analysis of the effect of zirconium precursors of MOF-808 on its thermal stability, and structural and surface properties, *CrystEngComm*, 2019, **21**, 1407–1415.

41 X.-M. Li, Y. Wang, Y. Mu, J. Gao and L. Zeng, Oriented construction of efficient intrinsic proton transport pathways in MOF-808, *J. Mater. Chem. A*, 2022, **10**, 18592–18597.

42 F. Vermoortele, B. Bueken, G. Le Bars, B. Van de Voorde, M. Vandichel, K. Houthoofd, A. Vimont, M. Daturi, M. Waroquier, V. Van Speybroeck, C. Kirschhock and D. E. De Vos, Synthesis Modulation as a Tool To Increase the Catalytic Activity of Metal–Organic Frameworks: The Unique Case of UiO-66(Zr), *J. Am. Chem. Soc.*, 2013, **135**, 11465–11468.

43 H. Wu, Y. S. Chua, V. Krungleviciute, M. Tyagi, P. Chen, T. Yildirim and W. Zhou, Unusual and Highly Tunable Missing-Linker Defects in Zirconium Metal–Organic Framework UiO-66 and Their Important Effects on Gas Adsorption, *J. Am. Chem. Soc.*, 2013, **135**, 10525–10532.

44 H. Furukawa, F. Gándara, Y.-B. Zhang, J. Jiang, W. L. Queen, M. R. Hudson and O. M. Yaghi, Water Adsorption in Porous Metal–Organic Frameworks and Related Materials, *J. Am. Chem. Soc.*, 2014, **136**, 4369–4381.

45 B. Garai, V. Bon, F. Walenszus, A. Khadiev, D. V. Novikov and S. Kaskel, Elucidating the Structural Evolution of a Highly Porous Responsive Metal–Organic Framework (DUT-49(M)) upon Guest Desorption by Time-Resolved in Situ Powder X-ray Diffraction, *Cryst. Growth Des.*, 2021, **21**, 270–276.

46 G. C. Shearer, S. Chavan, S. Bordiga, S. Svelle, U. Olsbye and K. P. Lillerud, Defect Engineering: Tuning the Porosity and Composition of the Metal–Organic Framework UiO-66 via Modulated Synthesis, *Chem. Mater.*, 2016, **28**, 3749–3761.

47 K. D. Nguyen, S. Ehrling, I. Senkovska, V. Bon and S. Kaskel, New 1D chiral Zr-MOFs based on in situ imine linker formation as catalysts for asymmetric CC coupling reactions, *J. Catal.*, 2020, **386**, 106–116.

48 G. Wißmann, A. Schaate, S. Lilienthal, I. Bremer, A. M. Schneider and P. Behrens, Modulated synthesis of Zr-fumarate MOF, *Microporous Mesoporous Mater.*, 2012, **152**, 64–70.

49 R. Issa, F. A. Ibrahim, M. Al-Ghoul and M. Hmadeh, Controlled growth and composition of multivariate metal–organic frameworks-199 via a reaction-diffusion process, *Nano Res.*, 2021, **14**, 423–431.

50 X. Wang, Z. Xu, L. Li, Y. Zhao, R. Su, G. Liang, B. Yang, Y. Miao, W. Meng, Z. Luan, K. Li, H. Xi and R. Zou, NO_2 Removal under Ambient Conditions by Nanoporous Multivariate Zirconium-Based Metal–Organic Framework, *ACS Appl. Nano Mater.*, 2020, **3**, 11442–11454.

51 H. H. Mautschke, F. Drache, I. Senkovska, S. Kaskel and F. X. Llabrés i Xamena, Catalytic properties of pristine and defect-engineered Zr-MOF-808 metal organic frameworks, *Catal. Sci. Technol.*, 2018, **8**, 3610–3616.

52 P. Hirschle, T. Preiß, F. Auras, A. Pick, J. Völkner, D. Valdepérez, G. Witte, W. J. Parak, J. O. Rädler and S. Wuttke, Exploration of MOF nanoparticle sizes using various physical characterization methods – is what you measure what you get?, *CrystEngComm*, 2016, **18**, 4359–4368.

53 W. Zhou and H. F. Greer, What Can Electron Microscopy Tell Us Beyond Crystal Structures?, *Eur. J. Inorg. Chem.*, 2016, 941–950.

54 F. Drache, V. Bon, I. Senkovska, C. Marschelke, A. Synytska and S. Kaskel, Postsynthetic Inner-Surface Functionalization of the Highly Stable Zirconium-Based Metal–Organic Framework DUT-67, *Inorg. Chem.*, 2016, **55**, 7206–7213.

55 Ü. Kökçam-Demir, A. Goldman, L. Esrafili, M. Gharib, A. Morsali, O. Weingart and C. Janiak, Coordinatively unsaturated metal sites (open metal sites) in metal–organic frameworks: design and applications, *Chem. Soc. Rev.*, 2020, **49**, 2751–2798.

56 H. Phetmung, K. Musikapong and T. Srichana, Thermal analysis, structure, spectroscopy and DFT calculations of a pharmaceutical cocrystal of salicylic acid and salicylamide, *J. Therm. Anal. Calorim.*, 2019, **138**, 1207–1220.

57 T. Ebata, N. Mizuochi, T. Watanabe and N. Mikami, OH Stretching Vibrations of Phenol−(H2O)1 and Phenol−(H2O)3 in the S1 State, *J. Phys. Chem.*, 1996, **100**, 546–550.

58 A. C. T. Cursino, J. E. F. d C. Gardolinski and F. Wypych, Intercalation of anionic organic ultraviolet ray absorbers into layered zinc hydroxide nitrate, *J. Colloid Interface Sci.*, 2010, **347**, 49–55.

59 N. Assaad, G. Sabeh and M. Hmadeh, Defect Control in Zr-Based Metal–Organic Framework Nanoparticles for Arsenic Removal from Water, *ACS Appl. Nano Mater.*, 2020, **3**, 8997–9008.

60 S. Dissegna, R. Hardian, K. Epp, G. Kieslich, M.-V. Coulet, P. Llewellyn and R. A. Fischer, Using water adsorption measurements to access the chemistry of defects in the metal–organic framework UiO-66, *CrystEngComm*, 2017, **19**, 4137–4141.

61 T. Sawano, N. C. Thacker, Z. Lin, A. R. McIsaac and W. Lin, Robust, Chiral, and Porous BINAP-Based Metal–Organic Frameworks for Highly Enantioselective Cyclization Reactions, *J. Am. Chem. Soc.*, 2015, **137**, 12241–12248.

62 Y. Peng, H. Huang, Y. Zhang, C. Kang, S. Chen, L. Song, D. Liu and C. Zhong, A versatile MOF-based trap for heavy metal ion capture and dispersion, *Nat. Commun.*, 2018, **9**, 187.

63 K. D. Nguyen, C. Kutzscher, S. Ehrling, I. Senkovska, V. Bon, M. de Oliveira, T. Gutmann, G. Buntkowsky and S. Kaskel, Insights into the role of zirconium in proline functionalized metal–organic frameworks attaining high enantio- and diastereoselectivity, *J. Catal.*, 2019, **377**, 41–50.

64 W. Zhang, J.-M. Yang, R.-N. Yang, B.-C. Yang, S. Quan and X. Jiang, Effect of free carboxylic acid groups in UiO-66 analogues on the adsorption of dyes from water: Plausible mechanisms for adsorption and gate-opening behavior, *J. Mol. Liq.*, 2019, **283**, 160–166.

65 M. J. Uddin, R. E. Ampiaw and W. Lee, Adsorptive removal of dyes from wastewater using a metal–organic framework: A review, *Chemosphere*, 2021, **284**, 131314.

66 H. Molavi, A. Hakimian, A. Shojaei and M. Raeiszadeh, Selective dye adsorption by highly water stable metal–organic framework: Long term stability analysis in aqueous media, *Appl. Surf. Sci.*, 2018, **445**, 424–436.

67 N. M. Mahmoodi, M. Oveisi, A. Taghizadeh and M. Taghizadeh, Synthesis of pearl necklace-like ZIF-8@chitosan/PVA nanofiber with synergistic effect for recycling aqueous dye removal, *Carbohydr. Polym.*, 2020, **227**, 115364.

68 Z. Chen, S. L. Hanna, L. R. Redfern, D. Alezi, T. Islamoglu and O. K. Farha, Reticular chemistry in the rational synthesis of functional zirconium cluster-based MOFs, *Coord. Chem. Rev.*, 2019, **386**, 32–49.

69 N. U. M. Nizam, M. M. Hanafiah, E. Mahmoudi, A. A. Halim and A. W. Mohammad, The removal of anionic and cationic dyes from an aqueous solution using biomass-based activated carbon, *Sci. Rep.*, 2021, **11**, 8623.

70 P. G. Saiz, N. Iglesias, B. González Navarrete, M. Rosales, Y. M. Quintero, A. Reizabal, J. Orive, A. Fidalgo Marijuan, E. S. Larrea, A. C. Lopes, L. Lezama, A. García, S. Lanceros-Mendez, M. I. Arriortua and R. Fernández de Luis, Chromium Speciation in Zirconium-Based Metal–Organic Frameworks for Environmental Remediation, *Chem. – Eur. J.*, 2020, **26**, 13861–13872.

71 Q. Chen, Q. He, M. Lv, Y. Xu, H. Yang, X. Liu and F. Wei, Selective adsorption of cationic dyes by UiO-66-NH2, *Appl. Surf. Sci.*, 2015, **327**, 77–85.

72 J. Liu, Y. Ye, X. Sun, B. Liu, G. Li, Z. Liang and Y. Liu, A multifunctional Zr(IV)-based metal–organic framework for highly efficient elimination of Cr(VI) from the aqueous phase, *J. Mater. Chem. A*, 2019, **7**, 16833–16841.

73 C. Zhang, Y. Liu, L. Sun, H. Shi, C. Shi, Z. Liang and J. Li, A Zwitterionic Ligand-Based Cationic Metal–Organic Framework for Rapidly Selective Dye Capture and Highly Efficient $Cr_2O_7^{2-}$ Removal, *Chem. – Eur. J.*, 2018, **24**, 2718–2724.

74 F. N. Azad, M. Ghaedi, K. Dashtian, S. Hajati and V. Pezeshkpour, Ultrasonically assisted hydrothermal synthesis of activated carbon–HKUST-1-MOF hybrid for efficient simultaneous ultrasound-assisted removal of ternary organic dyes and antibacterial investigation: Taguchi optimization, *Ultrason. Sonochem.*, 2016, **31**, 383–393.

75 E. Haque, J. E. Lee, I. T. Jang, Y. K. Hwang, J.-S. Chang, J. Jegal and S. H. Jhung, Adsorptive removal of methyl orange from aqueous solution with metal–organic frameworks, porous chromium-benzenedicarboxylates, *J. Hazard. Mater.*, 2010, **181**, 535–542.

76 L. Li, Z. Shi, H. Zhu, W. Hong, F. Xie and K. Sun, Adsorption of azo dyes from aqueous solution by the hybrid MOFs/GO, *Water Sci. Technol.*, 2016, **73**, 1728–1737.

77 E. Haque, J. W. Jun and S. H. Jhung, Adsorptive removal of methyl orange and methylene blue from aqueous solution with a metal–organic framework material, iron terephthalate (MOF-235), *J. Hazard. Mater.*, 2011, **185**, 507–511.

78 W. Lu, Z. Wei, Z.-Y. Gu, T.-F. Liu, J. Park, J. Park, J. Tian, M. Zhang, Q. Zhang, T. Gentle III, M. Bosch and H.-C. Zhou, Tuning the structure and function of metal–organic frameworks via linker design, *Chem. Soc. Rev.*, 2014, **43**, 5561–5593.

79 J.-M. Yang, A facile approach to fabricate an immobilized-phosphate zirconium-based metal–organic framework composite (UiO-66-P) and its activity in the adsorption and separation of organic dyes, *J. Colloid Interface Sci.*, 2017, **505**, 178–185.